



Article

Quantifying the Size-Dependent Shear Banding Behavior in High-Entropy Alloy-Based Nanolayered Glass

Kaiqing Dai ^{1,2} , Chun Zhang ^{1,2}, Wenjun Lu ³ and Jianjun Li ^{1,2,*}

¹ College of Mechanical and Electrical Engineering, Central South University, Changsha 410083, China; 203701021@csu.edu.cn (K.D.)

² State Key Laboratory of Precision Manufacturing for Extreme Service Performance, Central South University, Changsha 410083, China

³ Department of Mechanical and Energy Engineering, Southern University of Science and Technology, Shenzhen 518055, China

* Correspondence: mejjli@csu.edu.cn or jianjunli.mech@hotmail.com

Abstract: Extensive research has shown that nanolayered structures are capable of suppressing the shear banding in metallic glass in nanoindentation experiments. However, the specific mode and mechanism of the shear banding underneath the indenter remains unknown. Also, the quantification of shear banding-induced strain localization is still a challenge. Herein, the size-dependent shear banding behavior of a CuTiZrNb high-entropy alloy-based nanolayered glass with individual layer thicknesses (h) ranging from 5 to 80 nm was systematically investigated by nanoindentation tests. It was found that the hardness of the designed structure was almost size-independent. Yet, a clear transition in the deformation modes from the cutting-like shear bands to the kinking-like ones was discovered as h decreased to 10 nm. Moreover, multiple secondary shear bands also appeared, in addition to the primary ones, in the sample with $h = 10$ nm. The transition leads to an obvious strain delocalization, as clearly illustrated by the proposed theoretical model, which is based on the assumption of a pure shear stress state to quantify the shear banding-induced strain localization. The strain delocalization results from the higher density of amorphous/amorphous interfaces that exhibit the change in morphology with a refined layered glass structure.

Keywords: nanolayered glass; nanoindentation; shear banding; amorphous/amorphous interface



Citation: Dai, K.; Zhang, C.; Lu, W.; Li, J. Quantifying the Size-Dependent Shear Banding Behavior in High-Entropy Alloy-Based Nanolayered Glass. *Nanomaterials* **2024**, *14*, 546. <https://doi.org/10.3390/nano14060546>

Academic Editor: Kenji Kaneko

Received: 16 February 2024

Revised: 14 March 2024

Accepted: 15 March 2024

Published: 20 March 2024



Copyright: © 2024 by the authors. Licensee MDPI, Basel, Switzerland. This article is an open access article distributed under the terms and conditions of the Creative Commons Attribution (CC BY) license (<https://creativecommons.org/licenses/by/4.0/>).

1. Introduction

Metallic glass (MG) materials (or amorphous solids) usually possess ultra-high strength and hardness, due to their unique atomic structures lacking long-range orders, which prevents the initiation and motion of dislocations, as compared with their crystalline counterparts [1–6]. However, the lack of dislocation activities is the source of their near-zero plasticity since single shear banding-dominated deformation always generates catastrophic failure after the applied stress reaches the elastic limit of the material [7–10]. Therefore, improving the plasticity and tensile ductility of MGs while simultaneously maintaining their ultra-high strength has become an important issue in the field of materials science in recent decades [11–14]. Significant efforts have been made to achieve the above goal, and several typical and effective strategies based on interface engineering have emerged, which have generated the high density of crystalline/amorphous (C/A) and amorphous/amorphous (A/A) interfacial structures at the nanoscale [15–24].

The first effective strategy is to engineer MG-based composites by introducing ductile crystalline phases [25–35]. A typical example is a nanolayered 35 nm Cu/5 nm amorphous CuZr composite fabricated by magnetron sputtering [17]. The tensile test showed that the nanolayered composite exhibited a high flow stress of around 1.1 GPa and a tensile elongation to failure as high as 13.8%. The high tensile plasticity was attributed to the suppressed shear banding instability, due to the high-capacity sinks resulting from the

high density of C/A interfaces. Another typical example is the supra-nano C/A dual-phase magnesium alloy, in which 6 nm MgCu₂ nanocrystals were fully surrounded by 2 nm-thick magnesium-enriched amorphous shells [36]. This special C/A core-shell supra-nano structure enables the strongest magnesium alloy film with a near-ideal strength of 3.3 GPa by blocking the propagation of localized shear bands (SBs) in the C/A interfaces and dividing and rotating the nanocrystalline grains. Similar supra-nano structures and superior mechanical properties have also been achieved in an aluminum alloy [37] and a CrCoNi-Fe-Si-B high-entropy alloy (HEA) [38].

Another effective strategy is to develop various amorphous alloys with high density of nanoscale A/A interfaces by taking advantage of the size-dependent plasticity of MGs [12,16,18,23,39–42]. A typical amorphous material with nanoscale A/A interfaces is nanoglass [16,18,39,40,43–46], the microstructure of which is similar to that of nano-grained metals. However, the grain interior and boundary of the latter are replaced by the same amorphous phases but with different elemental contents. Many experiments and atomic simulations have shown that the plasticity of nanoglass materials can be substantially improved due to the nanoscale A/A interfaces [15,16,23,39–41,46,47]. For example, Wang et al. [48] produced a Sc₇₅Fe₂₅ nanoglass by the inert-gas condensation technique, which possessed nano-grains with a diameter of 10 nm and glassy interfacial regions with a thickness of 1 nm. The in situ tensile test of the designed nanoglass exhibited a plastic strain as high as 15%, while the MG counterpart showed almost no plasticity. Nandam et al. [43] prepared a Cu₅₀Zr₅₀ nanoglass with a particle size of 6 nm by using magnetron sputtering in an inert-gas condensation system, the compositions in the grain interior and interfacial regions of which were determined to be Cu₄₅Zr₅₅ and Cu₅₇Zr₄₃. The shear banding behavior was tested by microindentation, which showed that the shear banding observed in the nanostructure-free sample disappeared in the nanoglass sample. The homogeneous deformation and the enhanced resistance to the shear banding-induced strain delocalization was attributed to the interfacial regions of high free volume, which promotes the nucleation of many shear transformation zones (STZs).

In addition to experimental studies, molecular dynamics simulations have also been conducted to investigate the underlying deformation mechanisms of nanoglass with high plasticity [23,41,47,49]. For instance, Adibi et al. [47] studied the grain size-dependent Cu₅₀Zr₅₀ nanoglass with grain sizes varying from 15 to 5 nm by molecular dynamic simulations. The simulations revealed a transition from a single shear banding with a grain size larger than 10 nm to a homogeneous superplastic flow deformation with a grain size smaller than 5 nm. This transition originated from the uniformly distributed STZs and the homogeneous elastic energy release with grain refining.

Since the size of the grains and the thickness of the interfacial phase of nanoglass are difficult to adjust in the experiments of inert-gas condensation, a bottom-up method has been used to accurately control the A/A composites. A widely used bottom-up technique is magnetron sputtering (physical vapor deposition), which alternatively stacks nanoscale amorphous layers of different materials or compositions to form the designed composites [50–54]. For example, Sharma et al. [44] prepared a Zr₅₅Al₁₀Cu₃₀Ni₅/La₅₅Al₂₅Ni₁₀Cu₅Co₅ nanolayered glass (NLGs) with an individual layer thickness (*h*) of 200 nm by alternatively depositing the Zr-based and La-based amorphous targets in the magnetron sputtering system. It was found that the A/A layered interfaces completely suppressed shear banding in the amorphous alloy during nanoindentation tests, instead of the multiple SBs in the single-phase La-based or Zr-based MGs. The suppressed shear banding was believed to result from the blockage of SBs because of the existence of the A/A interfaces in the nanolayered structure. Recent experiments also showed that the shear banding behavior of nanolayered amorphous alloys was highly dependent on the layer thickness (i.e., the A/A interface spacing) [51,52,55]. For instance, Chen et al. [55] investigated the size effect of the nanoindentation behavior of Ni₆₀Nb₄₀/Zr_{50.7}Cu₂₈Ni₉Al_{12.3} NLGs. Their results showed that the shear banding was gradually suppressed with the decrease of *h*, and that the shear

banding fully disappeared in the samples with $h \leq 10$ nm. This enhanced homogeneous deformation might result from more and wavier A/A interfaces.

The above extensive experimental investigations have shown that the A/A interfacial structures can enable significant plasticity in amorphous alloys without sacrificing strength, which is suffered by the MG-based composites with C/A interfaces due to the incorporation of the relatively softer metallic phases [56]. However, most of the existing studies have focused on the shear banding-induced surface morphologies during the indentation process. What happened inside the materials underneath the indenter remains unclear, especially the specific characteristics of the SBs, including the shear banding mode (cutting-like or kinking-like SBs) [21]. Another important issue is that a theoretical model that can be used to quantify the shear banding-induced strain localization in the amorphous alloys is still lacking.

Herein, in order to address the above critical issues, a systematic study was conducted to investigate the effect of layer thickness on the shear banding behavior of a HEA-based NLG (i.e., $\text{Cu}_x(\text{TiZrNb})_{100-x}$ NLG) with a high density of nanoscale A/A interfaces by nanoindentation experiments. The nanoscale A/A interfacial structure is produced by alternatively co-sputtering Cu and TiZrNb targets under different sputtering powers for the two constituent layers. A combination of the detailed transmission electron microscopy (TEM) characterization of the indented areas and a theoretical analysis was employed. The results clearly show that the shear banding behavior is strongly dependent on the layer thickness, where the cutting-like shear banding is highly suppressed in the samples with refined layers. It was found that the decrease of layer thickness induces a transition of the shear banding mode, i.e., from the cutting-like SBs in the sample with $h = 80$ nm to a mixture of the cutting-like and kinking-like SBs in the sample with $h = 40$ nm, and finally to the kinking-like primary SBs accompanied by several secondary SBs in the sample with $h = 10$ nm. The theoretical analysis demonstrates that strain delocalization is enhanced with decreasing layer thickness in the $\text{Cu}_x(\text{TiZrNb})_{100-x}$ NLGs due to more and wavier A/A interfaces.

2. Materials and Methods

All $\text{Cu}_x(\text{TiZrNb})_{100-x}$ NLGs were obtained by co-sputtering Cu (99.99%) and TiZrNb (99.9%) targets on Si (100) substrates, which was achieved using a PTL6S PVD system at room temperature. Two constituent phases of the $\text{Cu}_x(\text{TiZrNb})_{100-x}$ NLGs are $\text{Cu}_{10}(\text{TiZrNb})_{90}$ and $\text{Cu}_{40}(\text{TiZrNb})_{60}$, respectively. These two phases have equal h , and the total thickness of all samples is 960 nm. The first layer of all samples is $\text{Cu}_{40}(\text{TiZrNb})_{60}$, and the top layer is $\text{Cu}_{10}(\text{TiZrNb})_{90}$. Before sputtering, the basic pressure inside the sputtering chamber was maintained below 6.5×10^{-5} Pa. During the sputtering process, Ar gas was supplied to stabilize the working pressure at 0.3 Pa. The two different components were realized by regulating the powers of the Cu target and TiZrNb target. The powers of the Cu target (TiZrNb target) used in the preparation of $\text{Cu}_{10}(\text{TiZrNb})_{90}$ and $\text{Cu}_{40}(\text{TiZrNb})_{60}$ components were 5 (150) and 30 (150) W, respectively, and the corresponding sputtering rates were 0.0110 (0.1649) and 0.0656 (0.1649) nm s^{-1} , respectively. To attain the uniform thickness and microstructure of the samples, the rotation speed of the substrate was maintained at 30 rpm during the sputtering process. The individual layer thicknesses of the composites were selected in the range from several to tens of nanometers (5–80 nm) in order to investigate the size-dependent shear banding behaviors of the HEA-based nanolayered glass.

In order to analyze the $\text{Cu}_x(\text{TiZrNb})_{100-x}$ NLGs, a series of characterizations were used, including X-ray diffraction (XRD, Bruker D8 Advance, Billerica, MA, USA), scanning electron microscopy (SEM, Tescan Mira 3, Brno, Czech Republic), and TEM (Talos F200X G2, Fulton, MD, USA) equipped with an energy dispersive spectroscopy (EDS) detector. TEM foils were prepared using a focused ion beam (FIB) system, specifically the FEI Helios Nanolab 600i. For evaluating the mechanical properties, a Nanoindenter system (Keysight, Agilent G200, Santa Clara, CA, USA) was employed to measure the hardness and shear instability of the $\text{Cu}_x(\text{TiZrNb})_{100-x}$ NLGs. The measurements of the hardness and Young's

modulus were conducted under a continuous stiffness measurement mode based on the Oliver–Pharr method [57], with a total of 12 indentations acquired on each sample. The spacing between the indentations was 25 μm . The maximum depth of indentation was 400 nm, and a consistent strain rate of 0.05 s^{-1} was maintained in all indentation tests.

3. Results and Discussion

3.1. Microstructures of the $\text{Cu}_x(\text{TiZrNb})_{100-x}$ NLGs

The structures of all the as-prepared samples were first analyzed by XRD. As shown in Figure 1, the XRD patterns of the $\text{Cu}_{10}(\text{TiZrNb})_{90}$ monolayer film, $\text{Cu}_{40}(\text{TiZrNb})_{60}$ monolayer film, and $\text{Cu}_x(\text{TiZrNb})_{100-x}$ NLGs with $h = 5\text{--}80$ nm only present broad amorphous diffraction peaks without sharp crystal peaks, indicating that all samples are composed of amorphous structures.

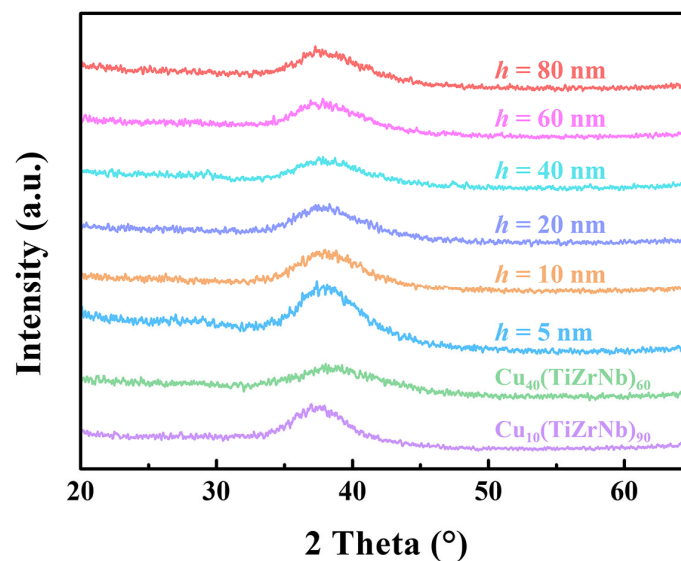


Figure 1. XRD patterns of the $\text{Cu}_{10}(\text{TiZrNb})_{90}$ monolayer film, $\text{Cu}_{40}(\text{TiZrNb})_{60}$ monolayer film, and $\text{Cu}_x(\text{TiZrNb})_{100-x}$ NLGs with different layer thicknesses.

High-angle annular dark-field scanning TEM (HAADF-STEM) and EDS were employed to investigate the internal structures and elemental distributions of three $\text{Cu}_x(\text{TiZrNb})_{100-x}$ NLGs with $h = 80, 40,$ and 10 nm. As displayed in Figure 2, it can be seen from the cross-sectional HAADF-STEM images that all samples have a layered modulation structure, and there is a conspicuous light and dark contrast between the two different phases. And all samples exhibit a perfect amorphous disordered structure, and no crystal particles are observed, which is well consistent with the above-mentioned XRD results. According to the HAADF-STEM measurements, the actual layer thicknesses of the $\text{Cu}_{10}(\text{TiZrNb})_{90}$ and $\text{Cu}_{40}(\text{TiZrNb})_{60}$ layers in the three $\text{Cu}_x(\text{TiZrNb})_{100-x}$ NLGs are 78.7 ± 0.5 and 78.9 ± 0.3 nm at $h = 80$ nm, 38.9 ± 0.5 and 39.0 ± 0.3 nm at $h = 40$ nm, and 8.3 ± 0.6 and 8.4 ± 0.7 nm at $h = 10$ nm, respectively, which are well in accord with the designed layer thicknesses. In addition, it can be demonstrated from the EDS mapping images (Figure 2b,d,f) that various elements are all uniformly distributed in the three $\text{Cu}_x(\text{TiZrNb})_{100-x}$ NLGs without any discernible element segregation, and all samples have a chemically alternating layer structure consisting of alternately stacked Cu-rich and Cu-poor layers. Moreover, in order to further verify the actual composition of the two phases, the $\text{Cu}_{10}(\text{TiZrNb})_{90}$ and $\text{Cu}_{40}(\text{TiZrNb})_{60}$ monolayer films were tested by EDS. The results (Figure 2g,h) manifest that the atomic percentages of Cu in the two phases are 11.7 at% and 38.9 at%, respectively, and the atomic percentages of Ti, Zr, and Nb in both phases are close to 1:1:1, which is within the error range of the design values.

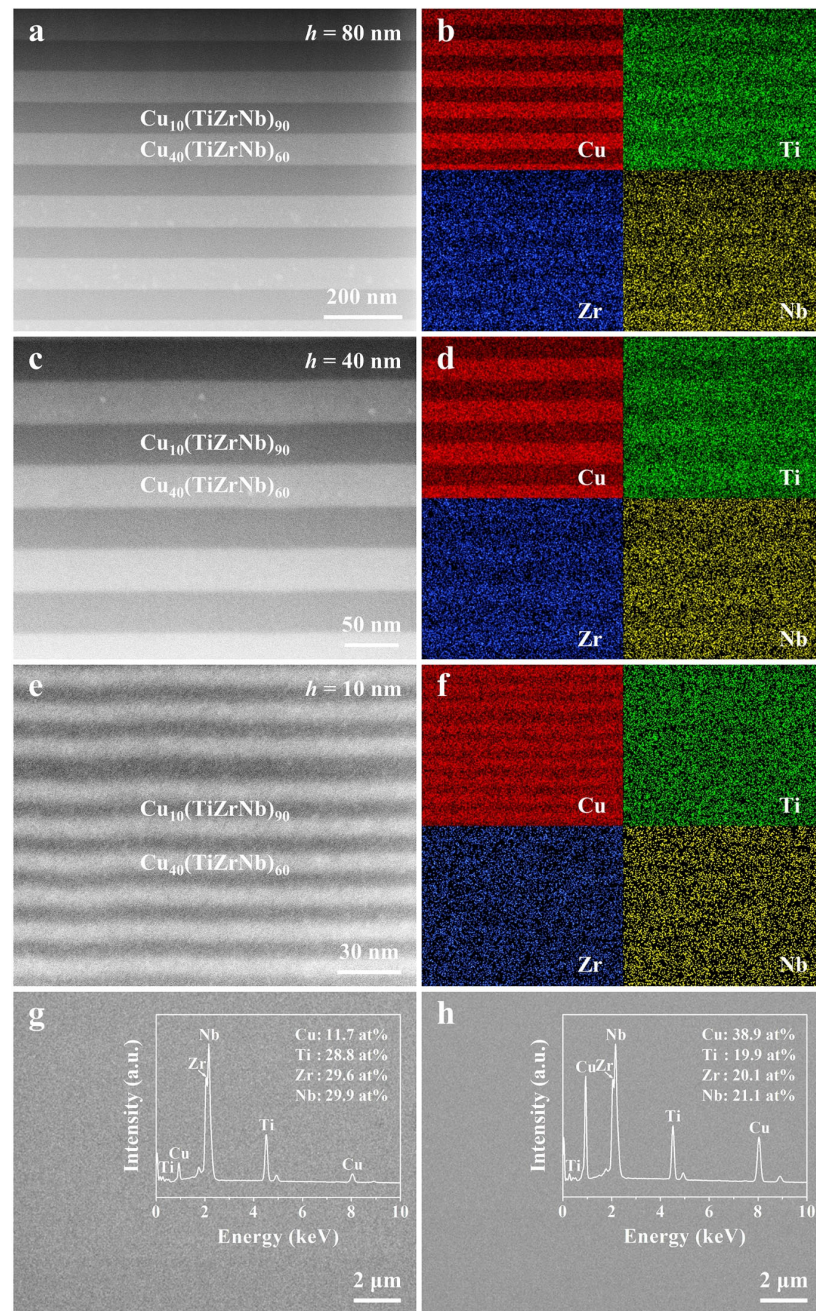


Figure 2. HAADF-STEM images and the corresponding EDS mapping images of the $\text{Cu}_x(\text{TiZrNb})_{100-x}$ NLGs with $h =$ (a,b) 80, (c,d) 40, and (e,f) 10 nm, respectively. SEM images and the corresponding EDS spectra of the (g) $\text{Cu}_{10}(\text{TiZrNb})_{90}$ and (h) $\text{Cu}_{40}(\text{TiZrNb})_{60}$ monolayer films, respectively.

In order to further characterize the details of the internal microstructures of the $\text{Cu}_x(\text{TiZrNb})_{100-x}$ NLGs, TEM, selected area electron diffraction (SAED), and high-resolution TEM (HRTEM) were applied. As depicted by Figure 3a–c and their insets, all three samples exhibit good amorphous structures, and the SAED patterns of the three samples only show typical amorphous rings without diffraction spots assigned to the crystal structure. Moreover, when $h = 80$ and 40 nm, the interlayer interfaces of the samples are almost straight (Figure 3d,e). But, as h decreases to 10 nm, wavy interlayer interfaces are observed (Figure 3f). This phenomenon of the interlayer interfaces gradually becoming wavier as the layer thickness decreases is similar to that of the reported $\text{Ni}_{60}\text{Nb}_{40}/\text{Zr}_{50.7}\text{Cu}_{28}\text{Ni}_9\text{Al}_{12.3}$ NLGs [55].

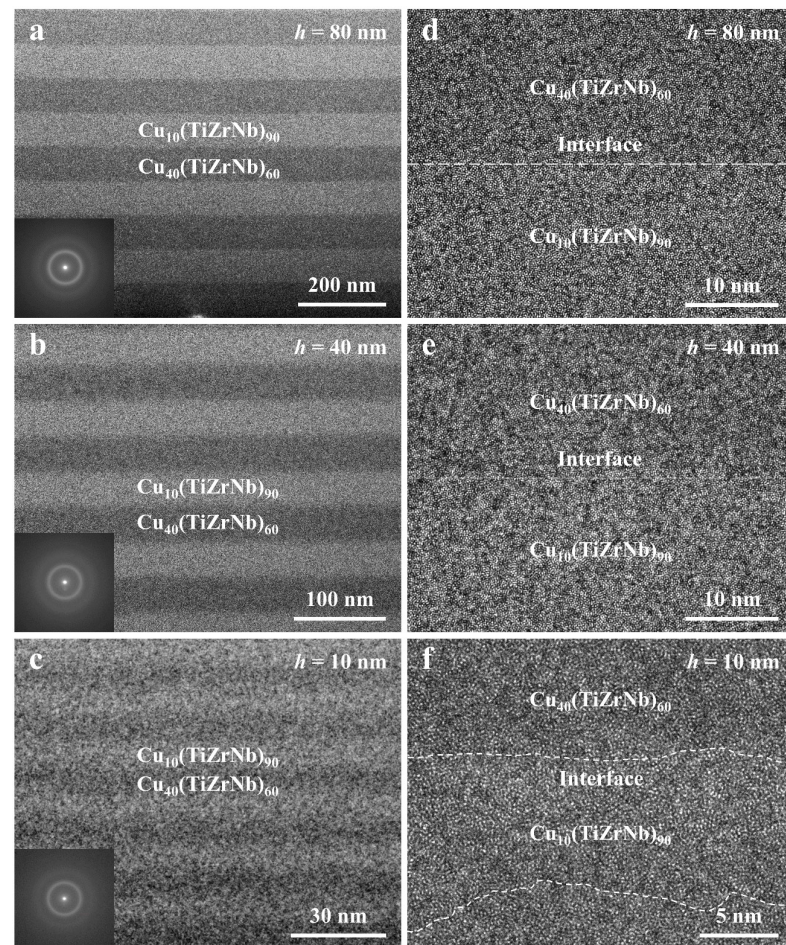


Figure 3. (a–c) The representative cross-sectional TEM images and (d–f) the corresponding HRTEM images of the $\text{Cu}_x(\text{TiZrNb})_{100-x}$ NLGs with $h = 80, 40,$ and 10 nm, respectively. Insets in (a–c) are the corresponding SAED patterns for the $\text{Cu}_x(\text{TiZrNb})_{100-x}$ NLGs. The white dashed lines in (d–f) represent the interfaces between two phases.

3.2. Mechanical Behaviors of the $\text{Cu}_x(\text{TiZrNb})_{100-x}$ NLGs

3.2.1. The Hardness of the $\text{Cu}_x(\text{TiZrNb})_{100-x}$ NLGs

The intrinsic hardness and elastic modulus of the $\text{Cu}_x(\text{TiZrNb})_{100-x}$ NLGs with different layer thicknesses as well as the $\text{Cu}_{10}(\text{TiZrNb})_{90}$ and $\text{Cu}_{40}(\text{TiZrNb})_{60}$ monolayer films were tested through nanoindentation experiments. From the hardness–indentation depth curves (Figure 4a) of the $\text{Cu}_x(\text{TiZrNb})_{100-x}$ NLGs, it can be seen that the hardness values of all samples first increase rapidly and then decrease with the increase of indentation depth. This can be attributed to the fact that the radius of the indenter and the surface roughness of the samples affect the hardness values at extremely shallow indentation depth [58,59]. When the indentation depth increases to the range of 100–180 nm, the hardness values plateau. Afterwards, due to the substrate effect, the hardness values continue to increase with the increase of indentation depth. Therefore, the corresponding plateau hardness values at indentation depths of 10–15% of the total thickness of the samples are regarded as the intrinsic hardness values of the samples. As shown in Figure 4b, it can be observed that the hardness of the $\text{Cu}_x(\text{TiZrNb})_{100-x}$ NLGs is not sensitive to changes in the layer thickness. Specifically, the hardness values of six samples with different layer thicknesses fluctuate within the range of 6.79–6.95 GPa. In addition, the hardness values of the six samples are higher than the hardness value of the $\text{Cu}_{10}(\text{TiZrNb})_{90}$ monolayer film but lower than the

hardness value of the $\text{Cu}_{40}(\text{TiZrNb})_{60}$ monolayer film. Based on the rule of mixture (ROM), the predicted hardness value of the $\text{Cu}_x(\text{TiZrNb})_{100-x}$ NLGs is obtained as follows:

$$H_{\text{ROM}} = f_{\text{Cu}_{10}(\text{TiZrNb})_{90}} H_{\text{Cu}_{10}(\text{TiZrNb})_{90}} + f_{\text{Cu}_{40}(\text{TiZrNb})_{60}} H_{\text{Cu}_{40}(\text{TiZrNb})_{60}} \quad (1)$$

where $f_{\text{Cu}_{10}(\text{TiZrNb})_{90}}$ and $f_{\text{Cu}_{40}(\text{TiZrNb})_{60}}$ are the volume fractions of the two phases, respectively, equal to 0.5, $H_{\text{Cu}_{10}(\text{TiZrNb})_{90}} = 6.63$ GPa, and $H_{\text{Cu}_{40}(\text{TiZrNb})_{60}} = 7.59$ GPa. The calculation result indicates that $H_{\text{ROM}} = 7.11$ GPa, which is higher than the actual hardness values of the six $\text{Cu}_x(\text{TiZrNb})_{100-x}$ samples. It is demonstrated from the above finding that the strengthening effect of the layered structure cannot be reflected in the $\text{Cu}_x(\text{TiZrNb})_{100-x}$ NLGs. Similar to the fact that the hardness values do not change significantly, the elastic modulus values fluctuate in the interval of 122.67–127.52 GPa when h changes in the range of 5–80 nm (Figure 4c,d).

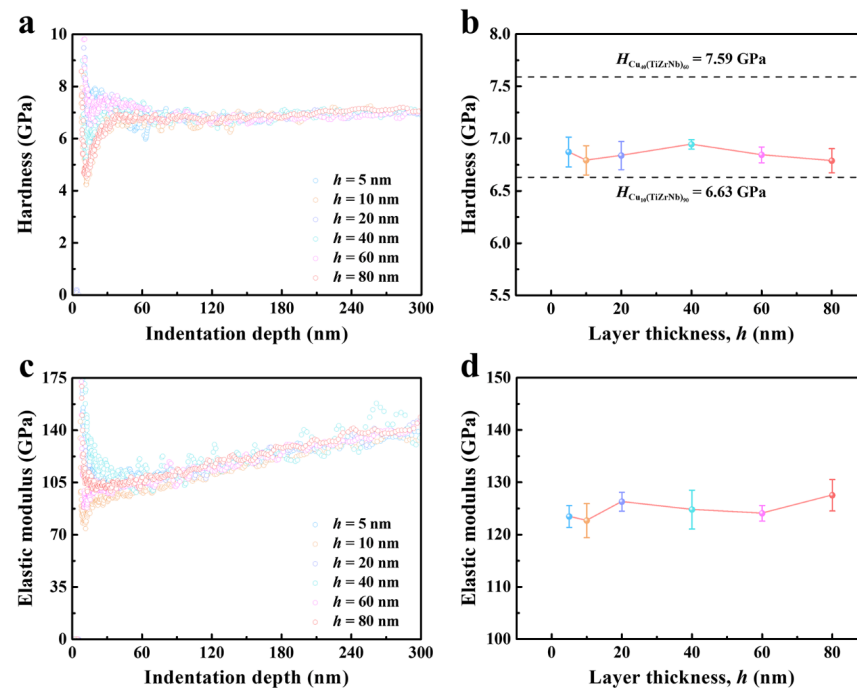


Figure 4. (a) The typical hardness–indentation depth curves and (b) the dependence of hardness on the layer thickness of the $\text{Cu}_x(\text{TiZrNb})_{100-x}$ NLGs. (c) The typical elastic modulus–indentation depth curves and (d) the dependence of elastic modulus on the layer thickness of the $\text{Cu}_x(\text{TiZrNb})_{100-x}$ NLGs.

3.2.2. The Shear Instability of the $\text{Cu}_x(\text{TiZrNb})_{100-x}$ NLGs

Following the nanoindentation experiments, SEM was utilized to investigate the residual indentation morphologies of the $\text{Cu}_x(\text{TiZrNb})_{100-x}$ NLGs with various layer thicknesses. From Figure 5a–f, it can be seen that at an indentation depth of 400 nm, well-shaped circular SBs appear on the indentation surfaces for all samples with $h = 5–80$ nm, as indicated by the white arrows. By analyzing the number of SBs, it is found that there is a strong dependence between the number of SBs and the layer thickness. That is, the number of SBs increases monotonically with the increase of layer thickness. Specifically, as shown in Figure 5g, the number of SBs on the indentation surfaces of the six $\text{Cu}_x(\text{TiZrNb})_{100-x}$ NLGs increases from 8 at $h = 5$ nm to 12 at $h = 80$ nm, implying that the shear instability increases monotonically with the increase of layer thickness.

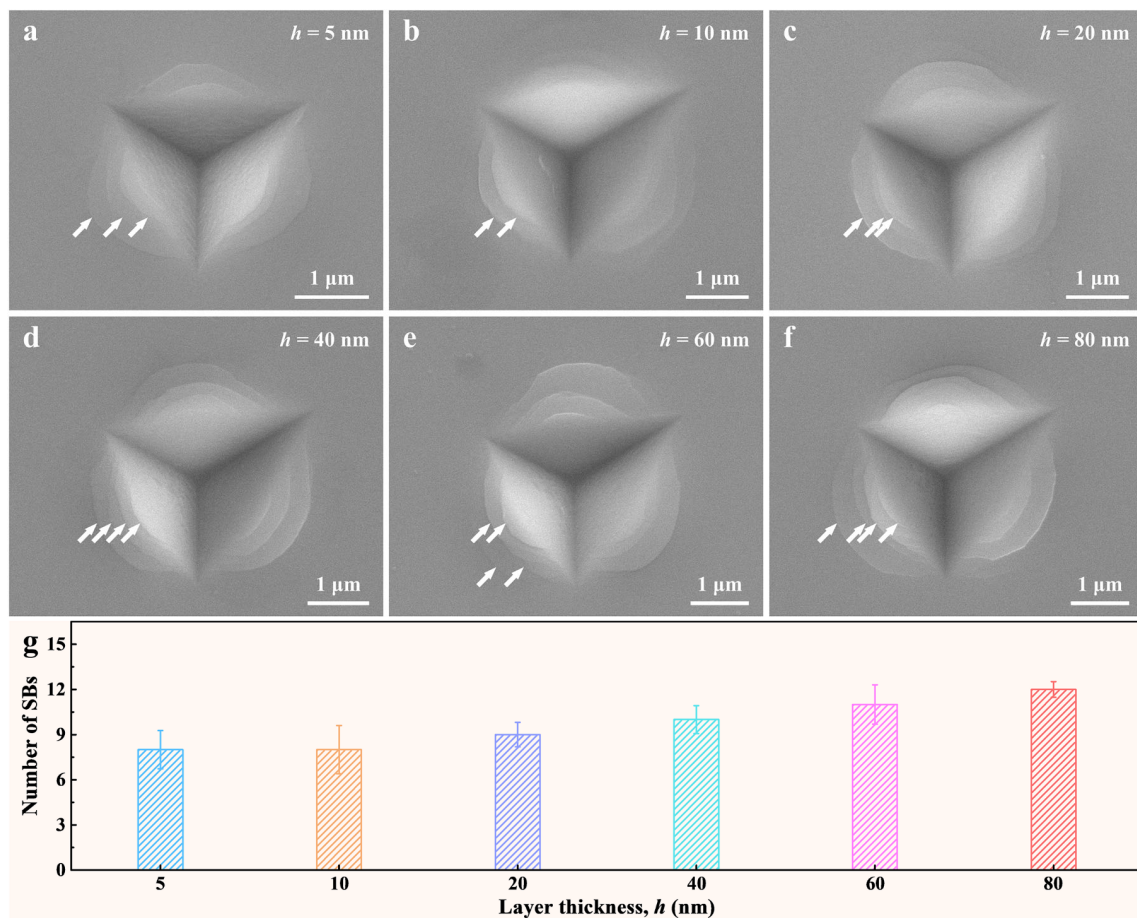


Figure 5. (a–f) SEM images of the indentations of the $\text{Cu}_x(\text{TiZrNb})_{100-x}$ NLGs with $h = 5$ –80 nm. The white arrows point to well-shaped circular SBs. (g) The number of SBs on the indentation surfaces of the $\text{Cu}_x(\text{TiZrNb})_{100-x}$ NLGs with different layer thicknesses.

In order to further analyze the deformation behaviors of the areas underneath the indenter and the SB areas near the indenter, the post-mortem TEM measurements were performed on the $\text{Cu}_x(\text{TiZrNb})_{100-x}$ NLGs with $h = 80$, 40, and 10 nm. Figure 6a presents the SEM image of the nanoindentation surface of the sample with $h = 80$ nm, and the white solid line represents the cross-sectional position used for preparing TEM lamellas by the FIB technique. For the $\text{Cu}_x(\text{TiZrNb})_{100-x}$ NLG with $h = 80$ nm, the obvious inhomogeneous thinning of the constituent layers is observed in the area underneath the indenter (Figure 6b,c). Consistent with the number of SBs on the nanoindentation surface observed by the SEM image, four SBs in the region next to the indenter are also revealed by the corresponding cross-sectional STEM image of the $\text{Cu}_x(\text{TiZrNb})_{100-x}$ NLG with $h = 80$ nm (Figure 6d). According to the distance between the SBs and the indenter, from near to far, the four SBs are named 80-SB1, 80-SB2, 80-SB3, and 80-SB4, respectively. The interlayer interfaces within the SBs underwent severe shear, forming sharp angles with the original horizontal direction (Figure 6e,f). This type of SB is defined as the cutting-like SB. Obviously, the four SBs are all cutting-like SBs that do not penetrate all constituent layers. The reason for the difference in deformation behaviors between the area underneath the indenter and the SB area next to the indenter is that the stress states in the two areas are different. Under ideal conditions, the area underneath the indenter is only subject to normal stress, which is consistent with the stress state in the micropillar compression test. In addition to the normal stress, there is also shear stress in the area next to the indenter, which is a complex stress state.

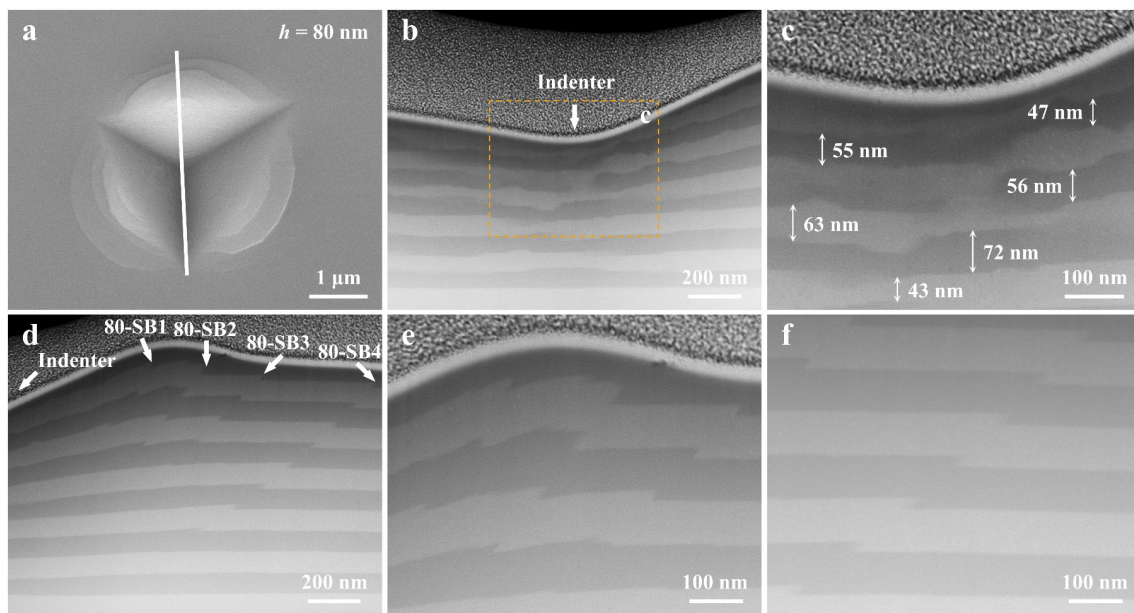


Figure 6. (a) SEM image and (b–f) the corresponding cross-sectional STEM images of the indentation of the $\text{Cu}_x(\text{TiZrNb})_{100-x}$ NLG with $h = 80$ nm. (b,c) show the deformation behavior underneath the indenter while (d–f) present the internal shear banding behavior, in which (c) is derived from the boxed region in (b) and (e,f) are amplified images from (d). The white solid line in (a) designates where the indentation was cross-sectioned. The positions of the indenter and the SBs are indicated by white arrows in (b,d).

Similar to the results at $h = 80$ nm, the $\text{Cu}_x(\text{TiZrNb})_{100-x}$ NLG with $h = 40$ nm exhibits several well-shaped circular SBs on the nanoindentation surface (Figure 7a). But unlike from the sample with $h = 80$ nm, the $\text{Cu}_x(\text{TiZrNb})_{100-x}$ NLG with $h = 40$ nm exhibits multiple SBs in the area underneath the indenter to accommodate the plastic deformation, as shown by the white arrows in Figure 7b. In addition, three SBs are identified in the area near the indenter (Figure 7c), and the number of SBs is consistent with that observed on the nanoindentation surface. According to the distance between the SBs and the indenter, from near to far, the three SBs are defined as 40-SB1, 40-SB2, and 40-SB3, respectively. Notably, the three SBs only penetrate a portion of the constituent layers and do not penetrate the entire sample. Unlike the case of the sample with $h = 80$ nm, the SBs formed in the sample with $h = 40$ nm in the area near the indenter are not all cutting-like SBs. Unlike the cutting-like SB formed by severe shear, the kinking-like SB is formed by the cooperative kinking of the constituent layers along the shear direction. Evidently, the 40-SB1 and 40-SB2 are a combination of the kinking-like and cutting-like SBs. The bottom of these two SBs displays the kink of the constituent layers, while severe shear occurs at the top of these two SBs. The 40-SB3 in all constituent layers are unified cutting-like SBs, as shown in the enlarged EDS image in Figure 7d. In summary, the $\text{Cu}_x(\text{TiZrNb})_{100-x}$ NLG with $h = 40$ nm exhibits different deformation modes in the areas underneath and adjacent to the indenter compared to the sample with $h = 80$ nm.

The $\text{Cu}_x(\text{TiZrNb})_{100-x}$ NLG with $h = 10$ nm exhibits a relatively small number of SBs on the nanoindentation surface (Figure 8a). Similar to the case of the sample with $h = 40$ nm, the plastic deformation of the $\text{Cu}_x(\text{TiZrNb})_{100-x}$ NLG with $h = 10$ nm is also accommodated by multiple SBs in the area underneath the indenter (Figure 8b). Moreover, three primary SBs can be observed in the area near the indenter, as indicated by the white arrows in Figure 8c, which is consistent with the number of SBs observed on the indentation surface. According to the distance between the SBs and the indenter, from near to far, the three primary SBs are named 10-SB1, 10-SB2, and 10-SB3, respectively. These three primary SBs are typical kinking-like SBs (Figure 8d), and none of them penetrate the entire sample. Significantly different from the first two samples, in addition to the primary SBs, many

secondary SBs are also observed in the sample with $h = 10$ nm, as indicated by the arrows in Figure 8e,f. The formation of secondary SBs is due to the fact that the formation of primary SBs is not enough to eliminate the stress of the surrounding matrix, and other locations still meet the yield conditions [8]. Therefore, the plastic deformation is accommodated by these secondary SBs together with primary SBs.

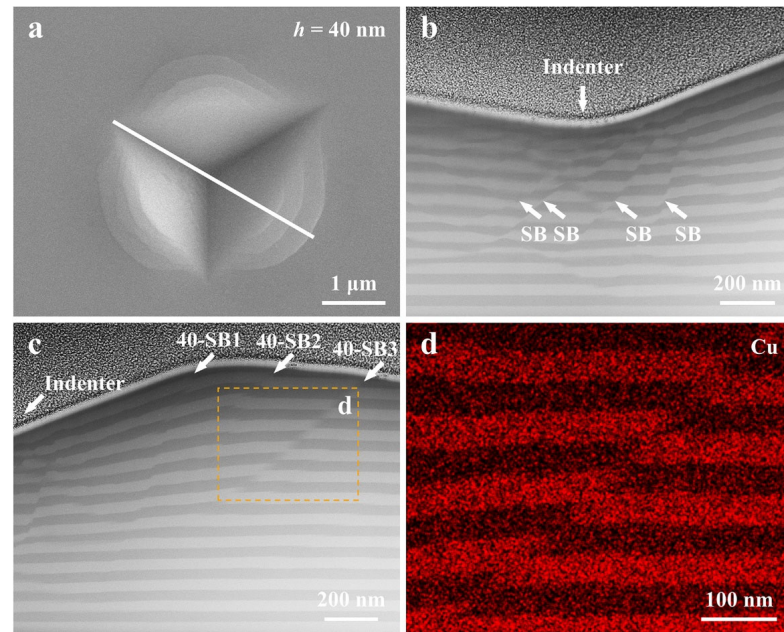


Figure 7. (a) SEM image, the corresponding cross-sectional (b,c) STEM images, and (d) EDS mapping image of the indentation of the $\text{Cu}_x(\text{TiZrNb})_{100-x}$ NLG with $h = 40$ nm. The white solid line in (a) represents where the indentation was cross-sectioned. (d) is derived from the boxed region in (c). The positions of the indenter and the SBs are indicated by white arrows in (b,c).

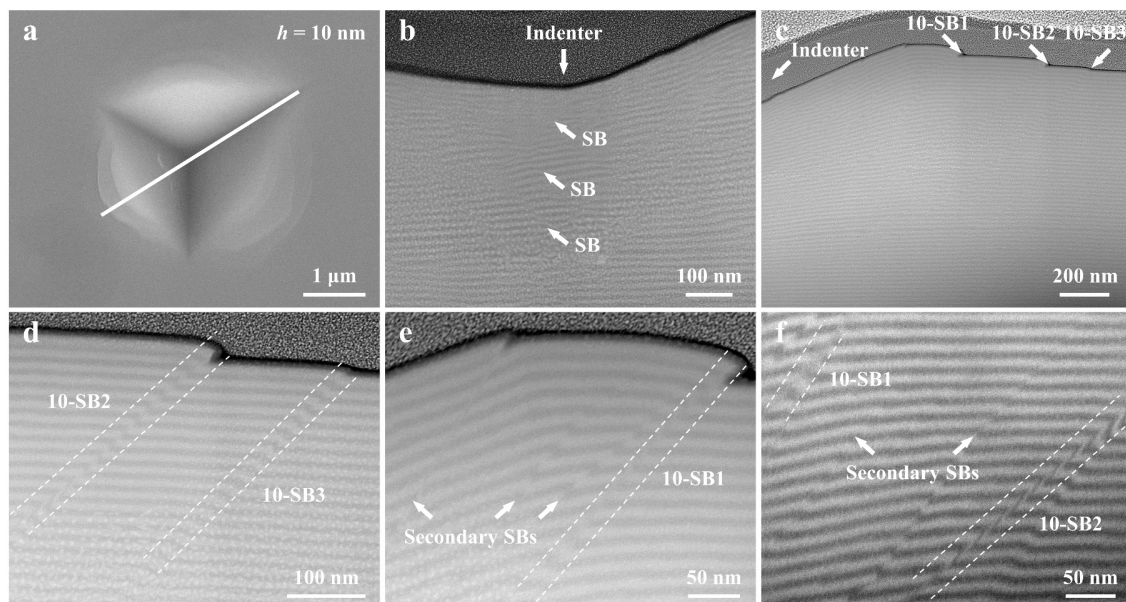


Figure 8. (a) SEM image, and (b–f) the corresponding cross-sectional STEM images of the indentation of the $\text{Cu}_x(\text{TiZrNb})_{100-x}$ NLG with $h = 10$ nm. The white solid line in (a) represents where the indentation was cross-sectioned. The positions of the indenter are indicated by white arrows in (b,c). The positions of SBs are indicated by white arrows and white dashed lines in (b–f).

The above results demonstrate that the deformation behaviors of the $\text{Cu}_x(\text{TiZrNb})_{100-x}$ NLGs in the areas underneath and near the indenter is highly correlated with the layer thickness. In the area underneath the indenter, the deformation behaviors of the $\text{Cu}_x(\text{TiZrNb})_{100-x}$ NLGs change from the non-uniform thinning of the constituent layers at $h = 80$ nm to multiple shear bandings at $h = 40$ and 10 nm as h decreases. Existing tensile and compression experiments have corroborated that the multiple shear banding behavior can make the deformation of MGs more uniform under uniaxial stress [48,60]. In the region near the indenter, the deformation behavior of the $\text{Cu}_x(\text{TiZrNb})_{100-x}$ NLGs changes from four cutting-like SBs at $h = 80$ nm to three SBs at $h = 40$ nm. And only the 40-SB3 is a complete cutting-like SB, and the other two SBs exhibit a combination of the kinking-like and cutting-like SBs. When h further decreases to 10 nm, three kinking-like primary SBs appeared, accompanied by multiple secondary SBs. A large number of nano/microindentation experiments have validated that the reduction in the number of SBs corresponds to the reduction in the shear instability of the sample under a complex stress state [21,43,55,61,62]. In addition, the shear instability of the cutting-like SBs is generally greater than that of the kinking-like SBs [21,61]. Thus, the shear instability resistance of the $\text{Cu}_x(\text{TiZrNb})_{100-x}$ NLGs gradually increases with the decrease of layer thickness. However, further precise quantitative analysis about the samples under three layer thicknesses is still needed to draw this conclusion.

In order to accurately quantify the degrees of shear instability within the SBs of the samples with different layer thicknesses, a theoretical model including two SB modes, i.e., the kinking-like and cutting-like SBs, was proposed based on the previous work of our group [21] (Figure 9). It was assumed that the SB region is subject to a pure shear stress state. According to the characteristics of the kinking-like and cutting-like SBs, they are simplified into geometric models, as shown in Figure 9a,b. Based on the microelement within the SB shown in Figure 9c, the shear strain (γ) is calculated as follows:

$$\gamma_i = \beta - \beta' = \varphi_i + \alpha - \frac{\pi}{2} \quad (2)$$

where i represents the i -th layer from bottom to top, α is the angle between the SB and the original interlayer interface, and φ is the kink angle between the interlayer interface within the SB and the original interlayer interface. Because φ is in the range of $[0, \pi - \alpha]$, the maximum value of γ is $\pi/2$ according to Formula (2). Moreover, since φ and α of the cutting-like SB are almost complementary (Figure 9b), the γ value of the cutting-like SB is close to the maximum value. In addition to γ , a new shear localization parameter (ζ_p) is also introduced in the model to characterize the degree of the shear localization of the SB. The calculation method is as follows:

$$\zeta_p = \frac{h_p}{w_{\text{SB}}} \quad (3)$$

where h_p and w_{SB} are the pile-up height induced by shear banding and the width of the SB, respectively.

Based on the models shown in Figure 9, the relevant parameters of the SBs of the $\text{Cu}_x(\text{TiZrNb})_{100-x}$ NLGs with $h = 80, 40,$ and 10 nm were measured, and $\alpha, w_{\text{SB}},$ and h_p are listed in Table 1. Of note, the SBs measured here are limited to those named previously, excluding multiple SBs in the area underneath the indenter and several secondary SBs. From Table 1, it can be seen that the α values of the SBs generated under these three layer thicknesses are all around 45° , which proves that the pure shear stress state assumed by the models is reasonable. Based on the measured φ of each layer, the shear strain values of each layer of the $\text{Cu}_x(\text{TiZrNb})_{100-x}$ NLGs with $h = 80, 40,$ and 10 nm were calculated. As shown in Figure 10a, for the cutting-like SBs (such as 80-SB1, 80-SB2, 80-SB3, and 80-SB4), the shear strain values of different layers are almost the same, that is, the φ values within the cutting-like SBs are almost constant. Furthermore, it can be seen through careful comparison that the shear strain of the sample with $h = 80$ nm is overall higher than that of the sample with $h = 40$ nm, and the shear strain of the sample with $h = 10$ nm is much lower

than that of the first two samples (Figure 10b). The maximum shear strain value (γ_{\max}) in each sample is selected as the criterion for judging the degree of shear instability of the sample. As shown in Figure 10c, the γ_{\max} values of the $\text{Cu}_x(\text{TiZrNb})_{100-x}$ NLGs with $h = 80, 40,$ and 10 nm are 1.55, 1.43, and 1.41, respectively, indicating that the degrees of shear instability of the $\text{Cu}_x(\text{TiZrNb})_{100-x}$ NLGs monotonically decrease with the decrease of h . The maximum values of strain localization parameter ($\zeta_{p,\max}$) for the $\text{Cu}_x(\text{TiZrNb})_{100-x}$ NLGs with $h = 80, 40,$ and 10 nm are 5.94, 4.75, and 4.29, respectively, implying that the degrees of shear instability are reduced by 28% when h decreases from 80 to 10 nm. Beyond that, the calculated $\zeta_{p,\max}$ values monotonically decrease with the decrease of h , which is consistent with the above-mentioned $\gamma_{\max} - h$ relationship. The above two parameters (i.e., γ_{\max} and $\zeta_{p,\max}$) jointly prove that the reduction of layer thickness improves the resistance to the shear instability of the $\text{Cu}_x(\text{TiZrNb})_{100-x}$ NLGs.

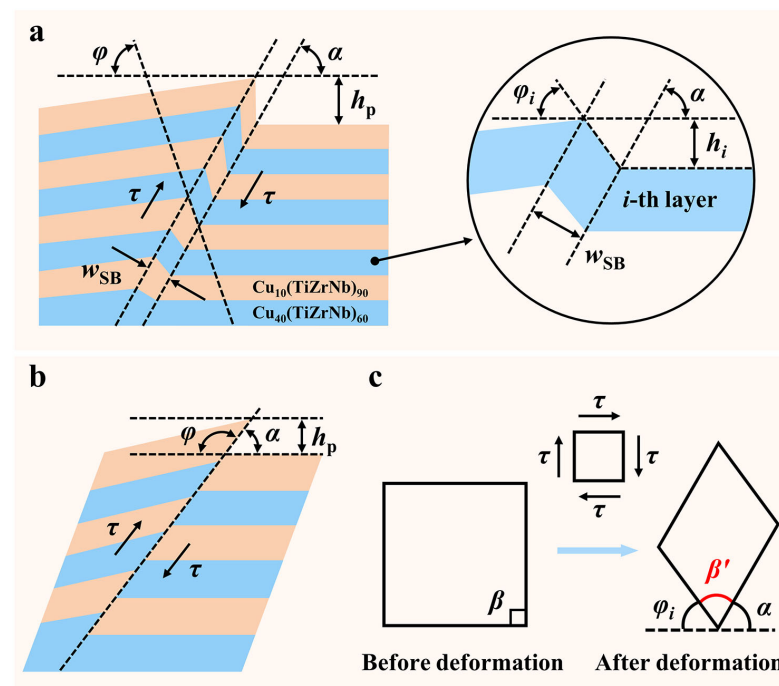


Figure 9. Schematic diagrams of the physical models of the (a) kinking-like and (b) cutting-like SBs, and (c) the corresponding microelement deformation within the given SB under a pure shear stress state in the $\text{Cu}_x(\text{TiZrNb})_{100-x}$ NLGs. In the above schematic diagram, β and β' are the angles before and after microelement deformation, respectively. The magnified image in (a) shows the geometric model details of the i -th layer, where h_i and φ_i are shear displacement and interface kink angle of the i -th layer within the SB, respectively.

Table 1. Summary of α , w_{SB} , and h_p for the $\text{Cu}_x(\text{TiZrNb})_{100-x}$ NLGs with $h = 80, 40,$ and 10 nm.

SB	α ($^\circ$)	w_{SB} (nm)	h_p (nm)
80-SB1	58	21	101
80-SB2	51	16	95
80-SB3	46	13	51
80-SB4	41	10	21
40-SB1	67	13	49
40-SB2	47	18	67
40-SB3	40	8	38
10-SB1	48	17	73
10-SB2	44	12	30
10-SB3	46	9	8

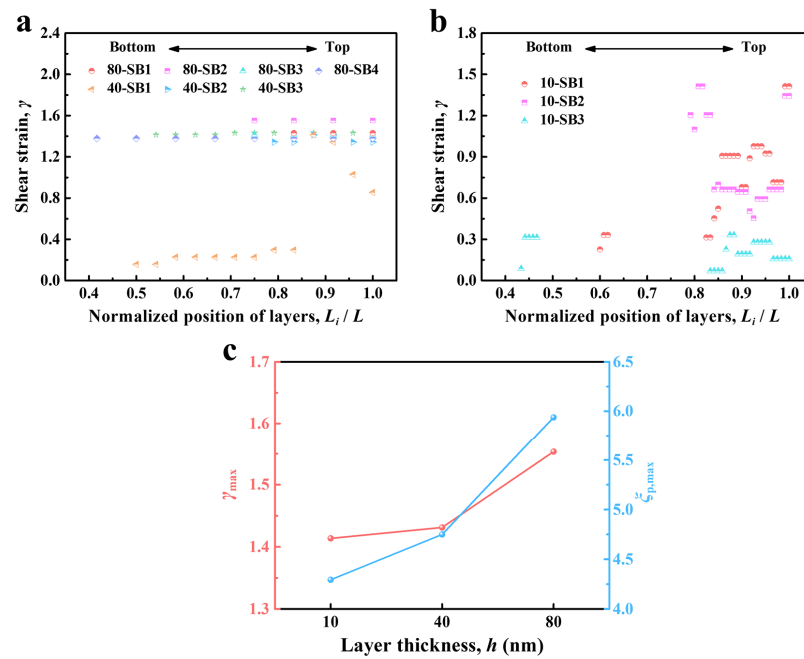


Figure 10. (a,b) The calculated γ within different SBs and (c) the corresponding calculated γ_{max} and $\zeta_{p,max}$ of the $\text{Cu}_x(\text{TiZrNb})_{100-x}$ NLGs with $h = 80, 40,$ and 10 nm, respectively. L_i/L denotes the normalized position of the constituent layers in each sample, where L_i is the position of the i -th layer from bottom to top and L is the total thickness of each sample.

As the layer thickness decreases, the reason for the transformation of the deformation modes and the enhancement of the resistance to shear instability is the increase in quantity and the change in the morphology of the A/A interfaces. As shown in Figure 11, stress concentration preferentially occurs at the A/A interfaces due to the high free volume of the A/A interfaces [63,64]. When the stress concentration reaches a certain level, STZs are activated [50,65]. These STZs will continue to diffuse along the direction of maximum shear stress within the constituent layers until reaching the next A/A interfaces. Due to the large layer thickness ($h = 80$ nm), the STZs need to penetrate fewer interfaces. Moreover, the A/A interfaces are straight, jointly making it easy for the STZs to penetrate the A/A interfaces and reach a critical size for generating mature SBs. Therefore, multiple cutting-like SBs appear in the region near the indenter for the $\text{Cu}_x(\text{TiZrNb})_{100-x}$ NLG with $h = 80$ nm.

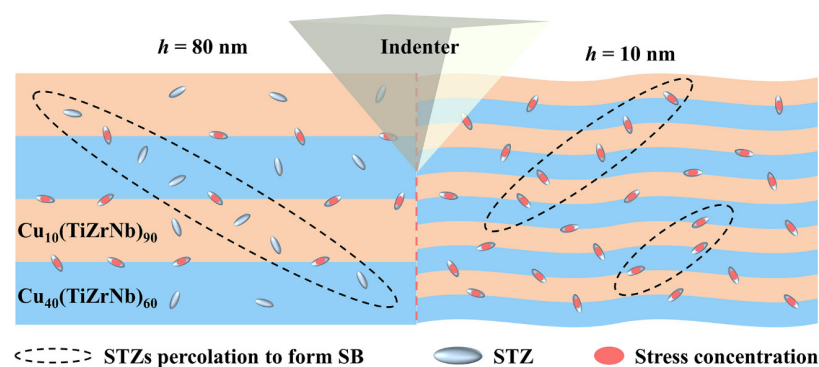


Figure 11. Schematic diagram of deformation mechanisms of the $\text{Cu}_x(\text{TiZrNb})_{100-x}$ NLGs with $h = 80$ and 10 nm under the nanoindentation experiments.

When $h = 10$ nm, the number of A/A interfaces increases significantly, and a large number of STZs appear in the interface regions. However, the formation of mature SBs needs to penetrate many interfaces, which greatly increases the resistance to the propagation of the SBs [55]. When the penetration of STZs is obstructed, they may first deviate along the

direction of A/A interfaces, and then penetrate in some relatively weak areas [66]. In this case, the mature SBs can also be formed in NLGs with smaller layer thickness. However, the interfaces of the $\text{Cu}_x(\text{TiZrNb})_{100-x}$ NLG with $h = 10$ nm are wavy, which may hinder the deflection of STZs and thus inhibit the formation of mature SBs. Therefore, in addition to the kinking-like primary SBs, a large number of secondary SBs appear in the area near the indenter to jointly accommodate the plastic deformation when $h = 10$ nm.

4. Conclusions

In this work, the $\text{Cu}_x(\text{TiZrNb})_{100-x}$ NLGs with different layer thicknesses were prepared by magnetron sputtering, and the layer thickness dependence of the deformation behaviors in the areas underneath and near the indenter in the nanoindentation experiments was systematically studied. Also, the degrees of shear instability of the samples with different layer thicknesses were accurately quantified through a theoretical model. The main conclusions are as follows:

- (1) The hardness and elastic modulus of the $\text{Cu}_x(\text{TiZrNb})_{100-x}$ NLGs are not sensitive to changes in the layer thickness. Specifically, in the range of $h = 5$ –80 nm, the values of hardness and elastic modulus of the six samples fluctuate within the ranges of 6.79–6.95 GPa and 122.67–127.52 GPa, respectively.
- (2) The deformation behaviors of the $\text{Cu}_x(\text{TiZrNb})_{100-x}$ NLGs in the areas underneath the indenter change with the decrease of layer thickness. In the areas underneath the indenter, the sample with $h = 80$ nm is deformed by the uneven thinning of the constituent layers, while the deformation of the samples with $h = 40$ and 10 nm is accommodated by multiple SBs.
- (3) In the areas near the indenter, the formed SBs are all cutting-like SBs for the $\text{Cu}_x(\text{TiZrNb})_{100-x}$ NLG with $h = 80$ nm, a combination of the cutting-like and kinking-like SBs is observed for the sample with $h = 40$ nm, and the kinking-like primary SBs and many secondary SBs are appeared in the sample with $h = 10$ nm.
- (4) The resistance to shear instability of the $\text{Cu}_x(\text{TiZrNb})_{100-x}$ NLGs increases monotonically with the decrease of layer thickness. When h decreases from 80 to 10 nm, the $\zeta_{p,\max}$ values of the samples decrease from 5.94 to 4.29. The improvement in shear instability resistance comes from the increase in the number of A/A interfaces and the A/A interfaces becoming wavier, which can effectively block the propagation of SBs.

In summary, the present experimental and theoretical studies clearly show that the shear banding-induced strong strain localization of the amorphous alloys can be significantly alleviated by introducing nanolayered structures. The underlying origin is the transition of deformation modes from cutting-like to kinking-like shear banding due to the refining of the nanolayered structure down to 10 nm. The advantage of the design is the creation of the unique homogeneous A/A interfaces that are produced by a single HEA system. This study provides an easy and flexible route to develop ultra-strong yet highly deformable amorphous alloys that could be widely employed in practical engineering applications. In addition, the proposed theoretical model provides a simple and convenient way to evaluate the strain localization of amorphous alloys in combination with simple nanoindentation tests that are easy to access by researchers.

Author Contributions: Methodology, data curation, validation, writing—original draft, K.D.; investigation, C.Z.; writing—review and editing, W.L.; conceptualization, resources, supervision, writing—review and editing, funding acquisition, J.L. All authors have read and agreed to the published version of the manuscript.

Funding: This work was financially supported by the National Natural Science Foundation of China (NSFC) (grant No. 12272413) and the Department of Science and Technology of Hunan Province, China (grant No. 2021RC3022).

Data Availability Statement: Data are contained within the article.

Conflicts of Interest: The authors declare no conflicts of interest.

References

1. Trexler, M.M.; Thadhani, N.N. Mechanical properties of bulk metallic glasses. *Prog. Mater. Sci.* **2010**, *55*, 759–839. [[CrossRef](#)]
2. Cheng, Y.; Ma, E. Atomic-level structure and structure–property relationship in metallic glasses. *Prog. Mater. Sci.* **2011**, *56*, 379–473. [[CrossRef](#)]
3. Yang, Y.; Zhou, J.; Zhu, F.; Yuan, Y.; Chang, D.J.; Kim, D.S.; Pham, M.; Rana, A.; Tian, X.; Yao, Y. Determining the three-dimensional atomic structure of an amorphous solid. *Nature* **2021**, *592*, 60–64. [[CrossRef](#)] [[PubMed](#)]
4. Ashby, M.; Greer, A.L. Metallic glasses as structural materials. *Scripta Mater.* **2006**, *54*, 321–326. [[CrossRef](#)]
5. Meyers, M.A.; Mishra, A.; Benson, D.J. Mechanical properties of nanocrystalline materials. *Prog. Mater. Sci.* **2006**, *51*, 427–556. [[CrossRef](#)]
6. Nguyen, T.A.K.; Dang, N.M.; Lin, C.-H.; Lee, M.-C.; Wang, Z.-Y.; Tsai, Y.-C.; Lin, M.-T. Effects of RF magnetron sputtering power on the mechanical behavior of Zr-Cu-based metallic glass thin films. *Nanomaterials* **2023**, *13*, 2677. [[CrossRef](#)]
7. Wang, W.-H.; Dong, C.; Shek, C. Bulk metallic glasses. *Mater. Sci. Eng. R* **2004**, *44*, 45–89. [[CrossRef](#)]
8. Schuh, C.A.; Hufnagel, T.C.; Ramamurty, U. Mechanical behavior of amorphous alloys. *Acta Mater.* **2007**, *55*, 4067–4109. [[CrossRef](#)]
9. Greer, A.; Cheng, Y.; Ma, E. Shear bands in metallic glasses. *Mater. Sci. Eng. R* **2013**, *74*, 71–132. [[CrossRef](#)]
10. Chen, D.; Dong, J.-F.; Ma, G.-Z. Synthesis and compressive fracture behavior of a CuZr-based bulk amorphous alloy with Ti addition. *J. Cent. S. Univ.* **2013**, *20*, 1137–1141. [[CrossRef](#)]
11. Wang, Z.T.; Pan, J.; Li, Y.; Schuh, C.A. Densification and strain hardening of a metallic glass under tension at room temperature. *Phys. Rev. Lett.* **2013**, *111*, 135504. [[CrossRef](#)]
12. Jang, D.; Greer, J.R. Transition from a strong-yet-brittle to a stronger-and-ductile state by size reduction of metallic glasses. *Nat. Mater.* **2010**, *9*, 215–219. [[CrossRef](#)]
13. Qiao, J.; Jia, H.; Liaw, P.K. Metallic glass matrix composites. *Mater. Sci. Eng. R* **2016**, *100*, 1–69. [[CrossRef](#)]
14. Qin, F.; Dai, K.; Chen, S.; Li, J. Nickel content-dependent microstructure and mechanical properties of TiZrNbHfNi high entropy alloy thin films. *Mater. Today Commun.* **2024**, *38*, 107932. [[CrossRef](#)]
15. Katnagallu, S.; Wu, G.; Singh, S.P.; Nandam, S.H.; Xia, W.; Stephenson, L.T.; Gleiter, H.; Schwaiger, R.; Hahn, H.; Herbig, M. Nanoglass–nanocrystal composite—A novel material class for enhanced strength–plasticity synergy. *Small* **2020**, *16*, 2004400. [[CrossRef](#)]
16. Gleiter, H. Nanoglasses: A new kind of noncrystalline material and the way to an age of new technologies? *Small* **2016**, *12*, 2225–2233. [[CrossRef](#)]
17. Wang, Y.M.; Li, J.; Hamza, A.V.; Barbee, T.W. Ductile crystalline-amorphous nanolaminates. *Proc. Natl. Acad. Sci. USA* **2007**, *104*, 11155–11160. [[CrossRef](#)]
18. Wang, Y.; Gleiter, H.; Li, M. From patterning heterogeneity to nanoglass: A new approach to harden and toughen metallic glasses. *MRS Bull.* **2023**, *48*, 56–67. [[CrossRef](#)]
19. Huang, Y.; Qin, F.; Dai, K.; Chen, S.; Li, J.; Li, J. Substantial toughening by thick nanoscale amorphous intergranular films in nanocrystalline materials. *J. Appl. Phys.* **2023**, *134*, 235101. [[CrossRef](#)]
20. Wang, Y.; Li, J.; Li, J.; Chen, S. On the strain delocalization mechanism of Cu/Nb nanolayered composites with amorphous interfacial layers. *Int. J. Plast.* **2024**, *172*, 103856. [[CrossRef](#)]
21. Qin, F.; Chen, F.; Hou, J.; Lu, W.; Chen, S.; Li, J. Strong resistance to shear instability in multilayered metallic composites by nanoscale amorphous-BCC crystalline interfaces. *Mater. Sci. Eng. A* **2024**, *891*, 145919. [[CrossRef](#)]
22. Kou, H.; Lu, J.; Li, Y. High-strength and high-ductility nanostructured and amorphous metallic materials. *Adv. Mater.* **2014**, *26*, 5518–5524. [[CrossRef](#)]
23. Sha, Z.D.; He, L.C.; Pei, Q.X.; Liu, Z.S.; Zhang, Y.W.; Wang, T.J. The mechanical properties of a nanoglass/metallic glass/nanoglass sandwich structure. *Scripta Mater.* **2014**, *83*, 37–40. [[CrossRef](#)]
24. Wang, H.; Chen, D.; An, X.; Zhang, Y.; Sun, S.; Tian, Y.; Zhang, Z.; Wang, A.; Liu, J.; Song, M. Deformation-induced crystalline-to-amorphous phase transformation in a CrMnFeCoNi high-entropy alloy. *Sci. Adv.* **2021**, *7*, eabe3105. [[CrossRef](#)]
25. Hofmann, D.C.; Suh, J.-Y.; Wiest, A.; Duan, G.; Lind, M.-L.; Demetriou, M.D.; Johnson, W.L. Designing metallic glass matrix composites with high toughness and tensile ductility. *Nature* **2008**, *451*, 1085–1089. [[CrossRef](#)]
26. Li, J.; Chen, H.; Feng, H.; Fang, Q.; Liu, Y.; Liu, F.; Wu, H.; Liaw, P.K. Microstructure evolution and deformation mechanism of amorphous/crystalline high-entropy-alloy composites. *J. Mater. Sci. Technol.* **2020**, *54*, 14–19. [[CrossRef](#)]
27. Liu, M.C.; Du, X.H.; Lin, I.C.; Pei, H.J.; Huang, J.C. Superplastic-like deformation in metallic amorphous/crystalline nanolayered micropillars. *Intermetallics* **2012**, *30*, 30–34. [[CrossRef](#)]
28. Luo, J.; Sun, W.; Liang, D.; Chan, K.C.; Yang, X.-S.; Ren, F. Superior wear resistance in a TaMoNb compositionally complex alloy film via in-situ formation of the amorphous-crystalline nanocomposite layer and gradient nanostructure. *Acta Mater.* **2023**, *243*, 118503. [[CrossRef](#)]
29. Pei, H.J.; Kuan, S.Y.; Liu, M.C.; Huang, J.C. Tensile behavior of amorphous/nanocrystalline ZrCu/Cu multilayered films with graded interfaces. *Intermetallics* **2012**, *31*, 191–195. [[CrossRef](#)]
30. Phan, T.; Rigelesaiyin, J.; Chen, Y.; Bastawros, A.; Xiong, L. Metallic glass instability induced by the continuous dislocation absorption at an amorphous/crystalline interface. *Acta Mater.* **2020**, *189*, 10–24. [[CrossRef](#)]
31. Yan, Z.; Liu, Z.; Yao, B.; An, Q.; Zhang, R.; Zheng, S. Effect of amorphous complexions on plastic deformation of nanolayered composites. *Scripta Mater.* **2023**, *231*, 115470. [[CrossRef](#)]

32. Zhang, J.Y.; Liu, G.; Sun, J. Self-toughening crystalline Cu/amorphous Cu-Zr nanolaminates: Deformation-induced devitrification. *Acta Mater.* **2014**, *66*, 22–31. [[CrossRef](#)]
33. Zhao, Y.F.; Chen, B.; Wang, Y.Q.; Zhang, J.Y.; Li, S.Z.; Wu, K.; Liu, G.; Sun, J. Size-dependent microstructural evolution and mechanical properties of crystalline/amorphous high-entropy alloy nanostructured multilayers: Cu/FeCoCrNiBSi vs Ni/FeCoCrNiBSi. *Acta Mater.* **2023**, *246*, 118706. [[CrossRef](#)]
34. Brandl, C.; Germann, T.C.; Misra, A. Structure and shear deformation of metallic crystalline–amorphous interfaces. *Acta Mater.* **2013**, *61*, 3600–3611. [[CrossRef](#)]
35. Wu, Y.; Xiao, Y.; Chen, G.; Liu, C.T.; Lu, Z. Bulk metallic glass composites with transformation-mediated work-hardening and ductility. *Adv. Mater.* **2010**, *22*, 2770–2773. [[CrossRef](#)]
36. Wu, G.; Chan, K.-C.; Zhu, L.; Sun, L.; Lu, J. Dual-phase nanostructuring as a route to high-strength magnesium alloys. *Nature* **2017**, *545*, 80–83. [[CrossRef](#)]
37. Wu, G.; Liu, C.; Sun, L.; Wang, Q.; Sun, B.; Han, B.; Kai, J.-J.; Luan, J.; Liu, C.T.; Cao, K. Hierarchical nanostructured aluminum alloy with ultrahigh strength and large plasticity. *Nat. Commun.* **2019**, *10*, 5099. [[CrossRef](#)]
38. Wu, G.; Balachandran, S.; Gault, B.; Xia, W.; Liu, C.; Rao, Z.; Wei, Y.; Liu, S.; Lu, J.; Herbig, M.; et al. Crystal–glass high-entropy nanocomposites with near theoretical compressive strength and large deformability. *Adv. Mater.* **2020**, *32*, 2002619. [[CrossRef](#)]
39. Sharma, A.; Nandam, S.H.; Hahn, H.; Prasad, K.E. On the differences in shear band characteristics between a binary Pd-Si metallic and nanoglass. *Scripta Mater.* **2021**, *191*, 17–22. [[CrossRef](#)]
40. Sharma, A.; Hirmukhe, S.S.; Nandam, S.H.; Hahn, H.; Singh, I.; Narayan, R.L.; Prasad, K.E. Strain rate sensitivity of a Cu₆₀Zr₄₀ metallic and nanoglass. *J. Alloys Compd.* **2022**, *921*, 165991. [[CrossRef](#)]
41. Sha, Z.; Branicio, P.; Pei, Q.; Liu, Z.; Lee, H.; Tay, T.; Wang, T. Strong and superplastic nanoglass. *Nanoscale* **2015**, *7*, 17404–17409. [[CrossRef](#)]
42. Pan, J.; Ivanov, Y.P.; Zhou, W.H.; Li, Y.; Greer, A.L. Strain-hardening and suppression of shear-banding in rejuvenated bulk metallic glass. *Nature* **2020**, *578*, 559–562. [[CrossRef](#)]
43. Nandam, S.H.; Ivanisenko, Y.; Schwaiger, R.; Śniadecki, Z.; Mu, X.; Wang, D.; Chellali, R.; Boll, T.; Kilmametov, A.; Bergfeldt, T.; et al. Cu-Zr nanoglasses: Atomic structure, thermal stability and indentation properties. *Acta Mater.* **2017**, *136*, 181–189. [[CrossRef](#)]
44. Sharma, P.; Yubuta, K.; Kimura, H.; Inoue, A. Brittle metallic glass deforms plastically at room temperature in glassy multilayers. *Phys. Rev. B* **2009**, *80*, 024106. [[CrossRef](#)]
45. Voigt, H.; Rigoni, A.; Boltynjuk, E.; Chellali, M.R.; Tyler, B.; Rösner, H.; Divinski, S.; Hahn, H.; Wilde, G. Evidence for glass–glass interfaces in a columnar Cu–Zr nanoglass. *Adv. Funct. Mater.* **2023**, *33*, 2302386. [[CrossRef](#)]
46. Wang, X.; Jiang, F.; Hahn, H.; Li, J.; Gleiter, H.; Sun, J.; Fang, J. Sample size effects on strength and deformation mechanism of Sc₇₅Fe₂₅ nanoglass and metallic glass. *Scripta Mater.* **2016**, *116*, 95–99. [[CrossRef](#)]
47. Adibi, S.; Sha, Z.-D.; Branicio, P.S.; Joshi, S.P.; Liu, Z.-S.; Zhang, Y.-W. A transition from localized shear banding to homogeneous superplastic flow in nanoglass. *Appl. Phys. Lett.* **2013**, *103*, 211905. [[CrossRef](#)]
48. Wang, X.L.; Jiang, F.; Hahn, H.; Li, J.; Gleiter, H.; Sun, J.; Fang, J.X. Plasticity of a scandium-based nanoglass. *Scripta Mater.* **2015**, *98*, 40–43. [[CrossRef](#)]
49. Zhao, Y.; Peng, X.; Huang, C.; Yang, B.; Hu, N.; Wang, M. Super ductility of nanoglass aluminium nitride. *Nanomaterials* **2019**, *9*, 1535. [[CrossRef](#)]
50. Doan, D.-Q.; Fang, T.-H.; Tran, T.-B.-T. Deformation behavior and strengthening mechanism of CuTa/CuTa amorphous/amorphous nanomultilayers. *J. Non-Cryst. Solids* **2023**, *600*, 121993. [[CrossRef](#)]
51. Huang, L.; Huang, P.; Wang, F. Excellent work-hardening in ZrCu/NiNb amorphous/amorphous nanolaminates. *Mater. Sci. Eng. A* **2022**, *831*, 142277. [[CrossRef](#)]
52. Huang, L.; Huang, P.; Wang, F. A new deformation mechanism of amorphous/amorphous laminates at deep nanoscale. *Mater. Sci. Eng. A* **2021**, *809*, 140923. [[CrossRef](#)]
53. Wu, G.; Liu, S.; Wang, Q.; Rao, J.; Xia, W.; Yan, Y.-Q.; Eckert, J.; Liu, C.; Ma, E.; Shan, Z.-W. Substantially enhanced homogeneous plastic flow in hierarchically nanodomained amorphous alloys. *Nat. Commun.* **2023**, *14*, 3670. [[CrossRef](#)]
54. Zhou, X.; Chen, C. Strengthening and toughening mechanisms of amorphous/amorphous nanolaminates. *Int. J. Plast.* **2016**, *80*, 75–85. [[CrossRef](#)]
55. Chen, Z.Q.; Li, M.C.; Cao, J.S.; Li, F.C.; Guo, S.W.; Sun, B.A.; Ke, H.B.; Wang, W.H. Interface dominated deformation transition from inhomogeneous to apparent homogeneous mode in amorphous/amorphous nanolaminates. *J. Mater. Sci. Technol.* **2022**, *99*, 178–183. [[CrossRef](#)]
56. Fan, Z.; Xue, S.; Wang, J.; Yu, K.Y.; Wang, H.; Zhang, X. Unusual size dependent strengthening mechanisms of Cu/amorphous CuNb multilayers. *Acta Mater.* **2016**, *120*, 327–336. [[CrossRef](#)]
57. Oliver, W.C.; Pharr, G.M.J. An improved technique for determining hardness and elastic modulus using load and displacement sensing indentation. *J. Mater. Res.* **1992**, *7*, 1564–1583. [[CrossRef](#)]
58. Bull, S.J.; Chen, J. Relation between the ratio of elastic work to the total work of indentation and the ratio of hardness to Young's modulus for a perfect conical tip. *J. Mater. Res.* **2009**, *24*, 590–598.
59. Chen, J.; Bull, S.J.; Roy, S.; Kapoor, A.; Mukaibo, H.; Nara, H.; Momma, T.; Osaka, T.; Shacham-Diamand, Y. Nanoindentation and nanowear study of Sn and Ni–Sn coatings. *Tribol. Int.* **2009**, *42*, 779–791. [[CrossRef](#)]

60. Xu, Y.-K.; Ma, H.; Xu, J.; Ma, E. Mg-based bulk metallic glass composites with plasticity and gigapascal strength. *Acta Mater.* **2005**, *53*, 1857–1866. [[CrossRef](#)]
61. Li, Y.P.; Zhu, X.F.; Tan, J.; Wu, B.; Zhang, G.P. Two different types of shear-deformation behaviour in Au–Cu multilayers. *Philos. Mag. Lett.* **2009**, *89*, 66–74. [[CrossRef](#)]
62. Gunti, A.; Jana, P.P.; Lee, M.-H.; Das, J. Effect of cold rolling on the evolution of shear bands and nanoindentation hardness in $Zr_{41.2}Ti_{13.8}Cu_{12.5}Ni_{10}Be_{22.5}$ bulk metallic glass. *Nanomaterials* **2021**, *11*, 1670. [[CrossRef](#)] [[PubMed](#)]
63. Demetriou, M.D.; Launey, M.E.; Garrett, G.; Schramm, J.P.; Hofmann, D.C.; Johnson, W.L.; Ritchie, R.O. A damage-tolerant glass. *Nat. Mater.* **2011**, *10*, 123–128. [[CrossRef](#)] [[PubMed](#)]
64. Guan, Y.; Wang, Y.; Song, W. Modulating mechanical performances of metallic amorphous materials through phase gradient. *Int. J. Mech. Sci.* **2022**, *234*, 107680. [[CrossRef](#)]
65. Delogu, F. Identification and characterization of potential shear transformation zones in metallic glasses. *Phys. Rev. Lett.* **2008**, *100*, 255901. [[CrossRef](#)]
66. Kuan, S.Y.; Chou, H.S.; Liu, M.C.; Du, X.H.; Huang, J.C. Micromechanical response for the amorphous/amorphous nanolaminates. *Intermetallics* **2010**, *18*, 2453–2457. [[CrossRef](#)]

Disclaimer/Publisher’s Note: The statements, opinions and data contained in all publications are solely those of the individual author(s) and contributor(s) and not of MDPI and/or the editor(s). MDPI and/or the editor(s) disclaim responsibility for any injury to people or property resulting from any ideas, methods, instructions or products referred to in the content.